Paper:

Monitoring of the Recovery Process of the Fukushima Daiichi Nuclear Power Plant from VHR SAR Images

Wen Liu*, Fumio Yamazaki*, and Tadashi Sasagawa**

*Graduate School of Engineering, Chiba University
1-33 Yayoi-cho, Inageku, Chiba 263-8522, Japan
E-mail: wen.liu@chiba-u.jp
**PASCO Corporation
4-10-1 Nakano, Nakano-Ku, Tokyo 164-0001, Japan
[Received October 10, 2015; accepted December 10, 2015]

The Mw9.0 earthquake hitting the Tohoku area on Japan's Pacific coast on March 11, 2011, triggered huge tsunamis and a Fukushima Daiichi nuclear power plant breakdown. Due to high radiation levels, plant damage could only be assessed from satellite images. Our study involves four very-high-resolution (VHR) TerraSAR-X/TanDEX-X SAR intensity images taken under different acquisition conditions and used to try and determine reactor building damage. Layover and radar shadow areas were specified first based on building footprint and height, then backscattering patterns in these areas were modeled by introducing sectional views of the target building. Criteria for detecting damage from individual SAR scenes were used to compare simulated backscattering patterns to actual SAR intensity images. Damage to other reactor buildings was then identified based on these criteria. Results were confirmed by comparisons to two optical VHR WorldView-2 images and ground photos.

Keywords: building damage, geometric features, WorldView-2, TerraSAR-X, TanDEM-X

1. Introduction

The epicenter of the Mw9.0 earthquake hitting Japan's northeastern Tohoku region on Japan's Pacific coast at 14:46 Japan standard time on March 11, 2011, was located at 38.30°N, 142.37°E, 60 km off of the coast. Tsunamis up to 40.5 m in runup height observed at Miyako, Iwate Prefecture, caused huge human loss and destroyed the regional infrastructure.

Tsunamis 13 to 15 m in maximum height struck the Fukushima Daiichi No.1 Nuclear Power Plant (NPP) 50 minutes after the main shock. Overtopping a 5.7 m seawall in front of the NPP, the waves flooded turbine building basements. They also disabled emergency diesel generators, at which point power and cooling systems stopped and several hydrogen explosions and meltdowns in three reactors occurred. These in turn caused a level 7 event on the international nuclear event scale (INES) [1].

The Fukushima Daini NPP 11 km south of the Daiichi NPP was also hit by a 9 m tsunami, which caused the reactor cooling water pumps to fail. One external high-voltage power line still functioned, however, to stabilize the reactors, avoiding meltdowns at the Daini NPP. Due to high radiation levels, the Japanese government ordered areas within 20 km of the Daiichi NPP and 10 km around the Daini NPP to be completely evacuated on March 12, 2011, making them no-entry zones. It was both difficult to grasp the situation from the ground and manned aerial surveys were banned until 2012. This left satellites and unmanned aerial vehicles (UAVs) as the only tools capturing the damage situations in these areas.

Optical images have been used to evaluate post-disaster areas both manually and automatically for over ten years [2–5]. Thanks to the very high resolution (VHR) of the newest optical satellites, e.g., QuickBird, GeoEye-1, and WorldView-2 and 3, it is now possible to classify the damage levels of individual buildings. Optical images are adversely affected by weather conditions and thus may not available immediately after a disaster occurs.

Synthetic aperture radar (SAR) operates under all weather conditions whether at day or night, so and hence satellites with SAR sensors become very useful in an emergency response. Multi-temporal SAR images taken before and after a disaster use interferometric coherence, intensity correlation, and change indices to detect damaged areas. Plank [6] comprehensively reviews these rapid damage assessment techniques. Matsuoka and Estrada [7] developed earthquake-induced building damage estimation models using ALOS PALSAR imagery to evaluate damage for the 2007 earthquake hitting Peru in South America. Improvements in spatial-resolution SAR sensors now enable high-resolution SAR images to be used in observing single buildings. We propose estimating building heights from a single TerraSAR-X (TSX) scene based on backscattering models [8]. Using one pre-event and two post-event TSX intensity images [9], we extract buildings in Miyagi Prefecture damaged in the Tohoku earthquake. However, the pre-event SAR images taken under the same acquisition condition as the post-event images are not available in many cases. Several studies have attempted to detect damage at the single-building level using both high-resolution optical and SAR

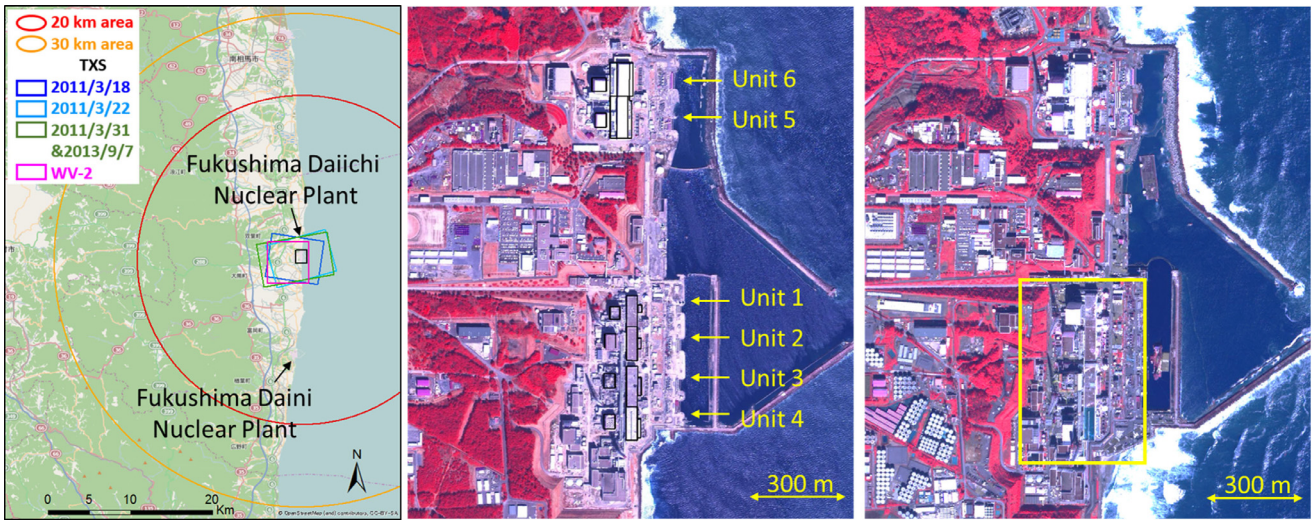

(a) The location of NPPs (b) WV-2 on 2011/03/28 (c) WV-2 on 2013/10/21

Fig. 1. The study area focus on the Fukushima Daiichi nuclear power plant, which locates along the coast of Fukushima Prefecture, Japan, with the cover ranges of the different satellite images (a); the false-color composites of WorldView-2 within the square of (a), taken on March 28, 2011 (b) and on October 21, 2013 (c), respectively.

images [10–11] In those studies, individual building dimensions obtained from a pre-event optical image were used to generate a simulated pre-event SAR backscattering model, then damaged building were estimated by comparing the simulated SAR image with the post-event image, but such research focused on evaluating building damage overall rather than the detailed damage of individual buildings.

In our study, we monitored damage conditions and recovery activities for Fukushima Daiichi NPP reactor buildings (R/Bs) by using four VHR TerraSAR-X and TanDEM-X intensity images taken after the earthquake. We simulated backscattering patterns within layover and radar shadow areas based on target building dimensions. Criteria on building damage were evaluated by comparing the simulated model to actual SAR intensity images, then classified uncovered R/Bs based on these criteria. We confirmed results by comparing them to the two optical VHR WorldView-2 images and ground photos.

2. Study Area and Image Data

2.1. Fukushima Daiichi Nuclear Power Plant

Our study focuses on the Fukushima Daiichi Nuclear Power Plant (NPP) shown in **Fig. 1(a)**, which is located in Okuma Town, Futaba County, Fukushima Prefecture. This NPP is operated by the Tokyo Electric Power Company (TEPCO) [12]. The six reactors, units 1-6, are divided into two groups, as shown in **Fig. 1(b)**. The first group contains units 1 to 4, from north to south. The second group, located north of the first group and on higher ground, includes units 5 and 6 from south to north. The first reactor, unit 1, started operation in March 1971 and the last, unit 6, began operation in October 1979. These light boiling water reactors (BWRs) generated about 30,000 GWh of electricity annually before the 2011 Tohoku earthquake, making it was one of the world's 15 largest NPPs. Units 7 and 8 were slated for construction in 2012 and 2013,but the project was cancelled after the 2011 accident.

Table 1. Acquisition conditions for the four TSX images used in this study.

Date	Incident angle	Heading angle	Path	Look direction
2011/03/18	49.4°	188.8°	Des.	right
2011/03/22	41.7°	344.9°	Asc.	left
2011/03/31	35.5°	349.8°	Asc.	right
2013/09/07	35.6°	349.8°	Asc.	right

2.2. Satellite Images and Preprocessing

WorldView-2 (WV-2), a commercial VHR optical satellite launched in October 2009, uses one 46-cm resolution panchromatic (PAN) and eight 1.85-m resolution multispectral (MS) bands. WV-2 images taken on March 28, 2011, and October 21, 2013, were used as part of ground truth data. We applied PC spectral sharpening [13] to obtain the 46-cm MS images shown in **Figs. 1(b-c)**.

TerraSAR-X (TSX), a commercial radar satellite launched in June 2007, uses an X-band with a 31-mm wavelength SAR antenna. The satellite captures data in five modes, ranging from 1-m HighSpot (HS) mode to 18.5-m spatial resolution ScanSAR mode. The revisit period – the time elapsing between observations of the same point on earth by a satellite – is from 2.5 to 11 days depending on imaging mode. In 2010, twin TSX and TanDEM-X satellites (TDX, an add-on for digital elevation measurement) were launched fly at a distance of a few hundred meters. TDX satellite specifications are almost identical to those of the TSX satellite [14].

In this study, we used four post-earthquake SAR images taken in HighSpot mode by HH polarization. Acquisition conditions are detailed in **Table 1**. The spatial

Table 2. Time series of events and activities for the units 1-4 from the earthquake on March 11, 2011 to Oct. 2013 based on [12].

Date	Unit 1	Unit 2	Unit 3	Unit 4
2011/03/11 (earthquake)	Working ⇒ Shut down	Working ⇒ Shut down	Working ⇒ Shut down	Shut down
2011/03/12	Explode at 15:36	Panel hole		
2011/03/14			Explode at 11:01	
2011/03/15			Explode again	Explode at 6:15
2011/06/28	Cover construction start			
2011/11/01	Cover construction complete			
2012/04/17				Cover construction start
2012/09			Debris removal start	
2013/03/11		Panel closing		
2013/07/20				Cover construction complete
2013/10/11			Debris removal complete	

resolution in the azimuth direction is 1.15 m and from 1.00 to 1.05 m in the range direction, depending on the incident angle. The first and second images taken by TSX, the third and fourth by TDX, were provided as enhanced ellipsoid corrected (EEC) products already orthorectifed and multilook-compressed by satellite owner DLR These products were then projected onto a World Geodetic System (WGS) 84 reference ellipsoid with a resampled square pixel size of 0.5 m. Image distortion caused by terrain height was compensated for by a globally available digital elevation model, the shuttle radar topography mission (SRTM).

Thanks to high orbit accuracy, these four intensity images overlapped correctly on the geo-map base without registration, so only radiometric calibration and a speckle filter were applied in preprocessing. The four SAR intensity images were transformed from a 16-bit digital number (DN) to the backscattering coefficient (sigma naught) in dB units based on the calibration factor. Incidence angle influence was removed in radiometric calibration, then an enhanced Lee filter [15] was applied to reduce speckle noise. Considering a balance between detail loss and speckle noise reduction, we used a 5×5 pixel window.

3. Fukushima Nuclear Accident and Response

Before the earthquake hit, units 4-6 had been shut down for refueling, but their spent-fuel pools still needed cooling. Units 1-3 shut down operation automatically immediately after the earthquake. Units 5 and 6 are separated from units 1-4 located on higher ground, so two unit 6 backup power generators surviving the tsunamis were sufficient for the cooling itself and neighboring reactor unit 5, which had been only slightly damaged. We selected units 1-4, which were the most damaged, for our study. Fuji-ie summarized this accident two weeks after the main shock [16].

Our study objective was building damage, so we selected events that changed building shape, summarized in **Table 2**. The first explosion, involving unit 1, occurred

(a) 2011/03/15 (b) 2011/03/21

(c) 2012/04/1

Fig. 2. Ground photos taken by the fixed cameras soon after the explosions published by Tokyo Electric Power Company (a-b) [12]; the side-looking aerial photograph taken by the GSI one year after the disaster (c) [17].

at 15:36 on March 12, the day after the main shock. The massive explosion blew away the concrete reactor building's roof and walls around the steel reactor vessel and injured 7 workers. The steel frame was exposed, which was confirmed from the optical satellite image as shown in **Fig. 1(b)**. This explosion also compromised the unit 2 wall and made a hole in the outer wall, which faced the sea. The next explosion, which was also massive, occurred at 11:01 on March 14 in unit 3, raising a large amount of flames and gray-brown smoke that rose higher than in the unit 1 explosion. This explosion collapsed the outer structure and covered the top of the reactor with debris. With the roof gone, debris was confirmed as shown in **Fig. 1(b)**. The blast adversely affected the unit 2 water supply and damaged unit 2. On March 15, further smoke from unit 3 was observed at 6:15. In the meantime, sounds of wall collapse were confirmed from unit 4, where the explosion damaged the fourth floor area above the reactor and the spent-fuel pool and deformed the outer structure. With the wall open due to the first explosion in unit 1,

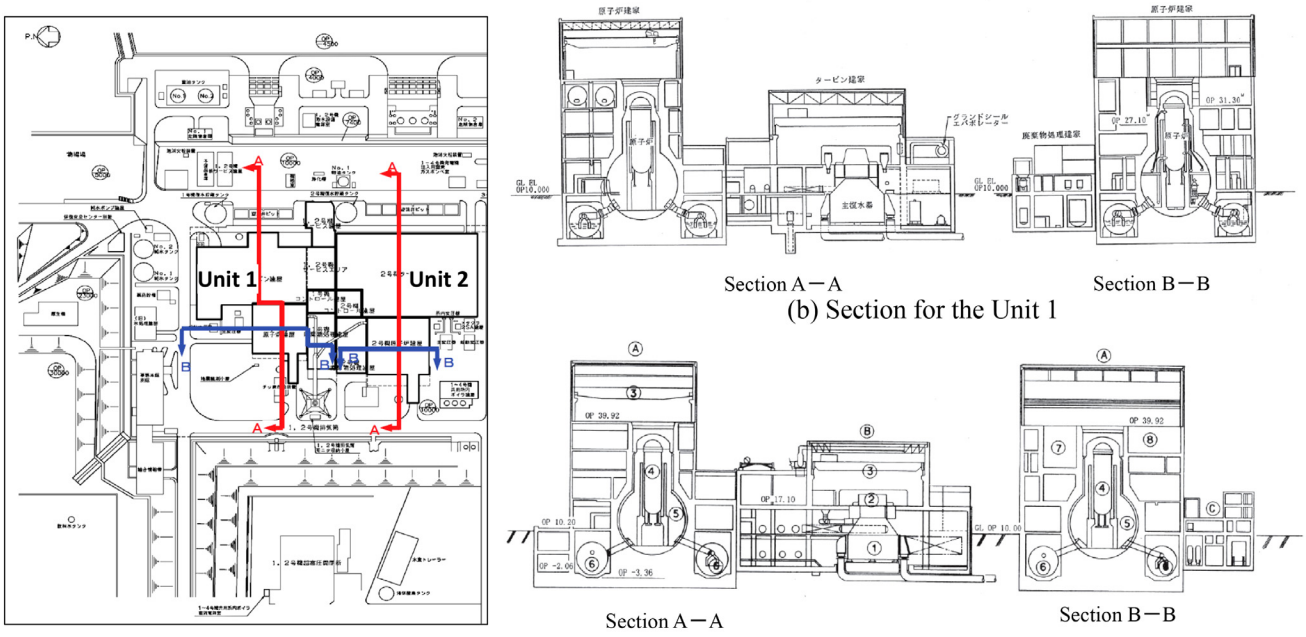

(a) Plan view for the Units 1 and 2

(b) Section for the Unit 1

(c) Section for the Unit 2

Fig. 3. Plan view for the location of the units 1 and 2 (a); the section views along the lines A-A and B-B for the unit 1 (b) and the unit 2 (c), respectively. All of those plans are cited from the report of TEPCO [12].

unit 2 avoided the massive explosion.

Figure 2(a) shows a fixed-camera shot of the NPP's inland side on March 15, 2011, uploaded on the TEPCO website [12], Note the different types of damage to units 1, 3 and 4. A closeup of units 3 and 4 taken on March 23 and shown in **Fig. 2(b)** shows unit 3's height reduced significantly due to the collapse of the top floors. The seaside wall's panels had been blown away by the explosion. Unlike units 1 and 3, the outer panels of unit 4 remained, although deformation to the roof and height was observed. All of the SAR images we used were taken after these explosions.

To help avoid the release of radioactive materials outside, a cover 54 m high, 47 m wide and 42 m deep was built for the unit 1 R/B, starting on June 28, 2011, and finishing on November 1, 2011, when it was completed. A side-looking aerial photograph taken by the Geospatial Information Authority of Japan on April 1, 2012, is shown in **Fig. 2(c)** [17], confirmed by the white gable roof. It also confirmed unit 2-4 damage shown from the seaside. The blown-out unit 2's R/B panel was closed on March 11, 2013, to reduce the unit's radioactive materials release. After several access trials from the ground, large debris on the top of unit 3 was removed between September 2012 and October 11, 2013. A cover was constructed for the unit 4 R/B starting on April 17, 2012, to remove fuel. Debris on the top of the building had been removed completely by July 11, 2012, and cover building construction was completed on July 20, 2013. The last SAR intensity image we used in this study was taken after the cover for units 1 and 4 had been constructed but before unit 3 debris had been removed. Recovery activities are also confirmed in the WV-2 image in **Fig. 1(c)**.

Table 3. The dimensions of the units 1-4 measured from the plans and sections [m] in [12].

Dimension	Unit 1	Unit 2	Unit 3	Unit 4
Wide (N-S)	39.4	45.1	45.1	45.1
Deep (E-W)	30.1	34.5	34.5	34.5
Height	43.4	47.0	46.1	46.1

4. Backscattering Model

We have worked on several research projects for detecting damage using geometric layover and radar shadows [18–21]. We used two post-event TSX intensity images for the Fukushima Daiichi NPP in StripMap mode to judge R/B damage [18]. Limited by spatial resolution, average backscatter differences in the layover area were not sufficient to detect building damage, but backscatter differences in shadow areas were sufficient for evaluating building height changes.

Thanks to the TSX/TDX sensor's very high resolution, especially in HighSpot mode, detailed variations in backscattering intensity within layover/shadow areas were observable in HS-mode images. We begin this study by discussing backscattering patterns for damaged and undamaged buildings, introducing target building dimensions. We then define the criteria for evaluating building damage from one SAR intensity image and the influence of the different acquisition conditions.

To build an accurate backscattering model, we used NPP building plans and sections. Those for units 1 and 2 are cited from a TEPCO report [12] and shown in **Fig. 3**. Each unit has one R/B and one turbine building. R/B dimensions for the sections of each unit are shown in **Table 3**. Turbine buildings are approximately 26 m high

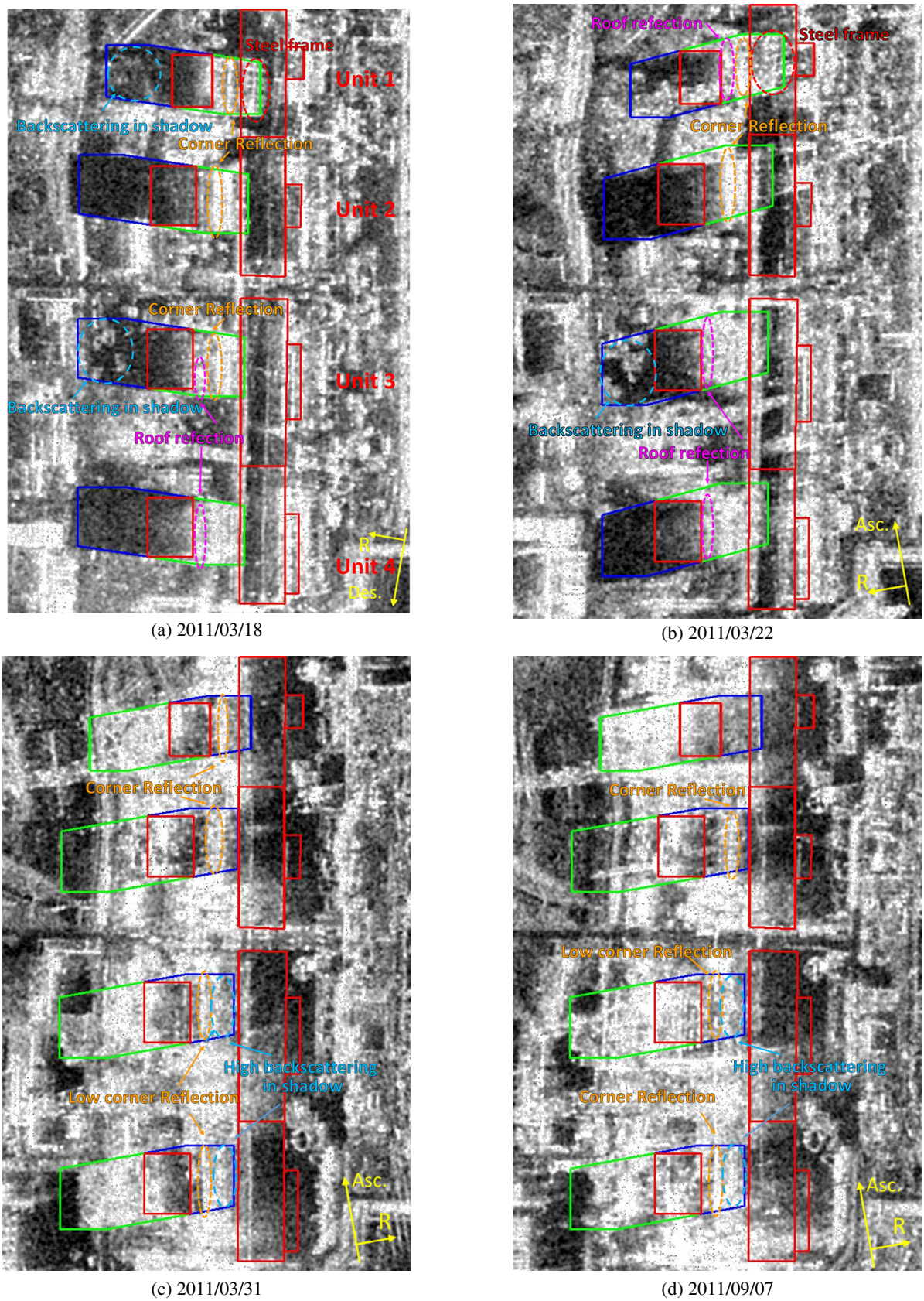

(a) 2011/03/18

(b) 2011/03/22

(c) 2011/03/31

(d) 2011/09/07

Fig. 4. TSX/TDX intensity images for the units 1-4 taken in the different acquisition conditions, with the footprints (red) and the layover (green)/shadow areas (blue) obtained according to the building heights.

above the ground. Footprints for individual units were made manually based on **Fig. 1(b)** and plans. They overlapped SAR intensity images along the red lines shown in **Fig. 4**. We then calculated layover and radar shadow areas based on acquisition conditions and building height. Layovers are indicated by green lines and radar shadows

by blue lines.

From plans and **Table 3**, we confirmed that unit 1's R/B was smaller and closer to the turbine building than other units. We selected units 1 and 2 as modeling examples, then simulated backscattering patterns within layovers and radar shadows based on sections. Using SAR simulation, we easily obtained backscatter intensity images from building models, but SAR simulation software is complicated and was not made available for us to use. Backscattering coefficients were not known for building materials, which depended on radar frequency and incident angle, so as a preliminary attempt, we simply simulated backscattering patterns using the following rule manually:

> *corner reflection* > *reflection from walls* > *reflection from roof and ground*

4.1. SAR Image on March 18, 2011

Based on the acquisition condition in **Table 1**, we found the incident angle to be 49.4° and the range direction to be 278.8° clockwise from the north. Since the incident angle is relatively large, layover is longer than that of the radar shadow. The layover length of unit 1's R/B was 37.2 m, whereas its radar shadow was 50.6 m long. The layover length of unit 2's R/B was 40.3 m whereas its radar shadow was 54.8 m long. R/B layovers overlapped turbine building (T/B) footprints. The backscattering pattern modeled along section A-A for units 1 and 2 is shown in **Fig. 5**.

Two lower buildings located between the unit 1 R/B and T/B and three buildings for unit 2 simplified the reflection pattern of unit 1. The strongest reflection comes from the corner between the R/B and connection buildings. The middle connection building for unit 2 is slightly higher than that of its neighboring seaside building as indicated by the second corner reflection shown in the unit 2 model. Backscattering from unit 1's R/B starts from one fifth of layover areas from west to east, overlapping the T/B's location. Most of the high backscattering intensity, however, is concentrated in the middle of the layover. The strongest corner reflection of the R/B for unit 2 is located one third of the layover area from the west. High backscatter intensity remains in layover areas until section corner reflection, which is located at the edge of the T/B location.

A model we built for damaged unit 1's R/B is shown in the lower plot in **Fig. 5(a)**. When top floors were blown up by explosions, the refection from the roof and upper walls was reduced. Due to the reflection of the new roof floor – now the top of the steel reactor vessel – backscatter intensity between the R/B footprint and corner reflection became longer. The new layover area starts from the inside of the R/B footprint. The radar shadow becomes shorter as the height of the roof changes, so there was some reflection within the original radar shadow area. The steel frame of the top floor still existed and reflected microwaves strongly, so backscattering from the steel frame appears in the eastern part of the layover.

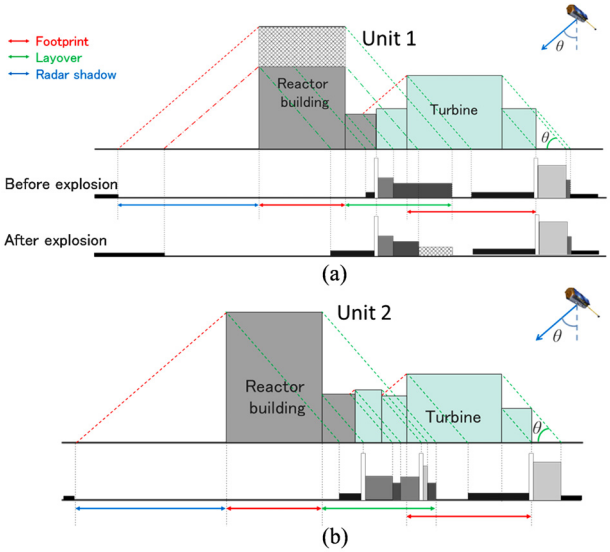

Fig. 5. Backscattering models for the TSX image taken on March 18, 2011 with 49.4° incident angle, along the section A-A in **Fig. 3**.

We compared backscatter models to the actual SAR intensity image in **Fig. 4(a)**. Thanks to the very high resolution of SAR data, the steel frame of unit 1's R/B is seen clearly in layover overlapping on the T/B. We identified one strong backscatter line between R/B and T/B footprints, which are considered to be the corner reflection from the R/B. Strong backscattering is also visible within the R/B footprint, representing reflection from the new roof. We confirmed reflections within the radar shadow based on reflections passing through the steel frame.

Although the unit 2 R/B seaside wall had been broken in the unit 1 explosion, the hole was too small to be identified within the SAR intensity image, so the unit 2 R/B was considered to not have been damaged. Strong backscattering was also seen between R/B and T/B footprints, which consisted of the corner reflection, reflection from the R/B seaside wall and reflection from the roof of the connecting building. Backscatter from the second corner reflection was not as significant as that in the layover overlapping the T/B footprint. Backscatter intensity between the R/B footprint and the first corner reflection was weak and there was little reflection in radar shadow areas. Based on these comparisons, our backscatter models showed good agreement with the actual SAR intensity image.

4.2. SAR Image on March 22, 2011

Based on acquisition conditions in **Table 1**, the incident angle was 41.7° and the range direction was 254.9° clockwise from the north. The incident angle was smaller than that of the March 18 image, so the layover was shorter and the radar shadow was longer. The unit 1's R/B layover was 48.7 m long and its radar shadow was 38.7 m long. The unit 2's R/B layover was 52.8 m long and its radar shadow was 41.9 m long. Most R/B layover overlapped on the location of T/Bs. The modeled backscattering pattern along section A-A for units 1 and 2 is shown in **Fig. 6**.

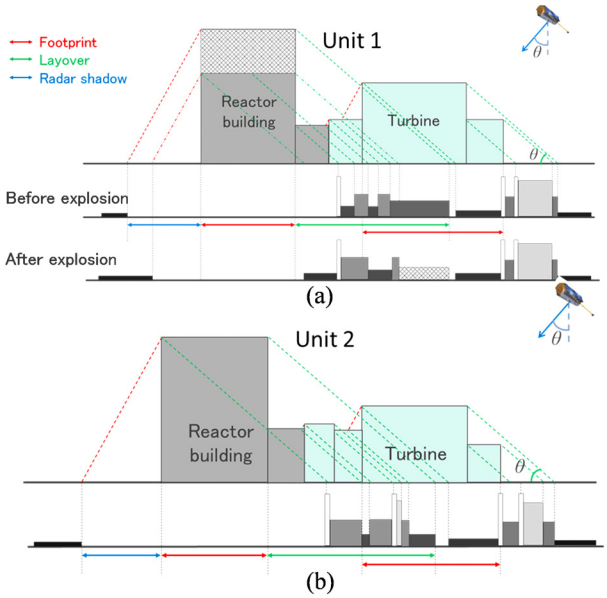

Fig. 6. Backscattering models for the TSX image taken on March 22, 2011 with 41.7° incident angle, along the section A-A in **Fig. 3**.

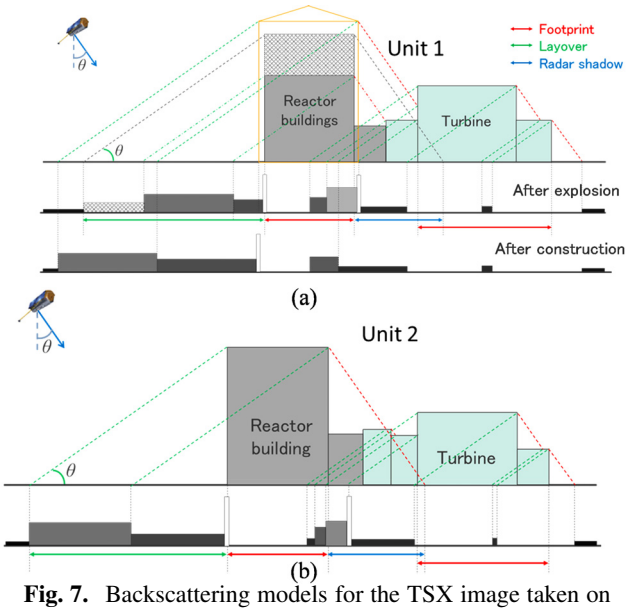

Fig. 7. Backscattering models for the TSX image taken on March 31, 2011 and September 7, 2013 with 35° incident angle, along the section A-A in **Fig. 3**.

The upper line in **Figs. 6(a)** and **(b)** is for the backscattering model for original buildings. Similar to models in the previous section, the strongest corner reflection was in the middle of the R/B and T/B, so high backscatter intensity was concentrated between the corner reflection and the east edge of layover. Although unit 1's R/B was closer to its T/B than the case for unit 2, the corner reflection was on the same line due to the different heights of connection buildings. Comparing unit 2 models, the backscatter intensity at the easternmost layover for the R/B is darker in **Fig. 6(b)** than in **Fig. 5(b)**. The model for damaged unit-1's R/B we built is shown as the lower line in **Fig. 6(a)**. Changes due to explosions are almost the same as for the model in **Fig. 5(a)**.

We compared these models to the actual SAR intensity image shown in **Fig. 4(b)**. In its different range direction, layover was directed toward the northeast. Corner reflections for unit 1 and 2 R/Bs were visible in the middle of R/B and T/B footprints. The unit-1 R/B's steel frame was also observable from this SAR image, and a low backscatter intensity area was observed near the east edge of the unit2 R/B's layover matching the model shown in **Fig. 6(b)**. High backscatter intensity in unit 1 radar shadow area shows in **Fig. 4(b)**, came from the reflection of an electric tower between units 1 and 2. Layover from the electric tower overlapped radar shadow area of the unit 1 R/B, making it was difficult to distinguish backscatter from the ground with reflection from the tower after the explosion. Under this acquisition condition, the radar shadow was not useful detecting damage.

4.3. SAR Images on March 31, 2011, and September 7, 2013

TDX images were taken on March 31, 2011, and September 7, 2013, under the same acquisition condition on an ascending path with the right look. The incident angle was about 35° and the range direction 79.8° clockwise from the north. Layover and radar shadow were directed opposite to those in the previous two TSX images, so inland-side walls were observed in these images. Due to the small incident angle, the layover was much longer than the radar shadow. The layover of the unit 1 R/B was 60.6 m long and the radar shadow was 31.1 m long, whereas the layover of the unit 2 R/B was 65.7 m long and the radar shadow was 33.7 m long. T/B layovers overlapped the radar shadow and R/B footprints. The modeled backscattering pattern along section A-A for units 1 and 2 is shown in **Fig. 7**.

The model of damaged unit 1 in the TDX image taken in 2011 is shown as the lower line of **Fig. 7(a)**. The strongest corner reflection occurred on the R/B footprint. There was a second corner reflection for the T/B in the R/B radar shadow area close to the footprint. A similar backscattering pattern exists in the unit 2 model. Two strong corner reflections around the footprint and in the middle of the R/B radar shadow. Unlike in observation from the seaside, the R/B layovers overlapped on the reflection from the ground, which is darker than the layover overlapping connection buildings. The reflection from the T/B overlapped the R/B radar shadow, so shadow areas also showed high backscattering.

We then compared these models to the SAR image in **Fig. 4(c)**. The two corner reflections for units 1 and 2 are easily identifiable, but the backscatter pattern within layovers did not match models. Reflections from the ground and objects on the west side of R/Bs were initial conditions in backscattering patterns. A lack of information about the west side of the R/B made modeling the backscattering difficult.

As stated in Section 3, the cover constructed for the unit 1 R/B was completed in November 2011. The model for the TDX image taken in 2013 was built and is shown as the upper line in **Fig. 7(a)**. Backscatter intensity in

the R/B layover became stronger after a solid wall with a steel frame was built. Due to the cover height, the corner reflection from the T/B disappeared in the radar shadow. Compared to **Fig. 4(d)**, both the increased backscattering in layover and the decrease in radar shadow were confirmed.

5. Damage Detection

In a comparison to models for the damaged unit 1 R/B and the undamaged unit-2 R/B to actual SAR intensity images, criteria for estimating building damage are summarized as follows:

1) Corner reflection
2) Reflection from the outer wall
3) Radar shadow

Corner reflection is identified most easily from a real SAR intensity image, so we used this as the first criterion. For the case in this study, corner reflection by the R/B should exist between R/B and T/B footprints when the SAR was observed from the seaside or around the R/B footprint observed from the inland side. If no corner reflection exists, it represents collapse of the entire building or debris covering the corner, then the wall reflection appeared between the corner reflection and the edge of the layover. These reflections usually overlap onto other surfaces, however, it is difficult to judge the backscattering intensity of the wall from one single scene due to the lack of information. A similar undamaged building must thus be used as the standard. If the wall is broken or has disappeared, backscatter intensity would decrease. If only the concrete cover has disappeared as in the case of unit 1, the high-resolution SAR intensity image shows the remaining steel frame as illustrated in **Figs. 4(a-b)**. We identified this type of damage by its skeleton pattern. Radar shadows have been proven to be efficient in estimating changes in height. If the original radar shadow is not overlapped by other reflections, backscattering within the radar shadow area represents damage to the target building directly. If the radar shadow area is overlapped by other reflections, a standard is needed to estimate the increase in intensity.

To detect unit 3 and 4 R/B damage, we applied the criteria 1), 2) and 3) above to the three SAR images taken in March 2011. Based on the plan view and **Table 3**, the distance between the R/B and T/B and dimensions of units 3 and 4 are similar to those of unit 2. This means that the models for unit 2 are usable in detecting damage.

First, we looked for corner reflections of R/Bs in **Fig. 4(a)**. Compared to the unit 2 corner reflection, weaker corner reflection occurs for unit 3 but no corner reflection occurs for unit 4. We observed backscatter between corner reflections and footprints of R/Bs (magenta) for units 3 and 4, representing the collapse of roof floors. To evaluate radar reflection from the wall, we used unit 2 that was apparently undamaged as the standard. Compared to backscatter intensity between the corner reflection and the edge of the layover, backscatter intensities for unit 3 and 4 R/Bs showed irregular patterns differing from those of unit 2, especially in the unit 4 region. We therefore concluded that damage could occur to the walls of R/Bs. We also considered that high backscatter intensity in the unit 3 R/B radar shadow area (cyan) had become lower than before. This matched the backscatter increase between the corner reflection and the footprint, but there is no significant reflection in the unit 4 R/B radar shadow, which means its height changed little.

We also conducted detection using **Figs. 4(b)** and **(c)**. In (b), corner reflections for unit 3 and 4 R/Bs could not be identified, thus representing the disappearance of the outer wall. The increases in backscatter intensity between the locations of the corner reflection and the footprint of R/Bs (magenta) was observed again, which were led by the decrease in building height. Backscattering patterns within the layover did not match our model for unit 2. These phenomena represent the damage to seaside walls of these R/Bs. The high backscatter intensity was also seen in unit 3 radar shadow (cyan) in this SAR image.

In **Fig. 4(c)**, it was difficult to evaluate backscatter patterns in layover areas due to the lack of information west of R/Bs, so we used the backscattering pattern in the radar shadow. Compared to unit 2 patterns, T/B corner reflections were weak for units 3 and 4. High backscattering areas within the radar shadow (cyan) were wider than those of unit 2, so we expected to find damage to roof floors. Observation from the west side was not as efficient as that from the east side. During comparison, we found that the SAR image taken on March 18, 2011, is best for detecting R/B damage at the Fukushima Daiichi NPP.

6. Recovery Activities

Note that we did not model recovery activities in this study because the September 7, 2013, SAR image was taken under the same acquisition conditions as the image taken on March 31, 2011. We calculated differences to monitor recovery using a 5×5 pixel smoothing window, which was the same size as the speckle filter. Obtained differences are shown in **Fig. 8**. R/B layover and radar shadow areas are shown in magenta and black frames.

Based on **Fig. 8**, we concluded that significant changes occurred in this target area. Average values of differences within the layover, footprint and radar shadow areas of the four R/Bs are summarized in **Table 4**. Compared to unit 2 that was not undergoing recovery work, backscatter intensity increased largely in unit 1 and 3 R/B layovers. Considering observations in the previous section, we found it difficult to directly link these increases to R/B recovery work. Significant changes in radar shadow areas for units 1 and 4 represent changes in building height. Cover construction for unit 1 and 4 R/Bs was completed before the SAR image acquired in 2013, these changes match progress in recovery activities. Backscatter intensity also changed significantly within R/B footprints, so recovery work was conducted for these units. We therefore could not asses the details of R/Bs without referring to the backscattering model.

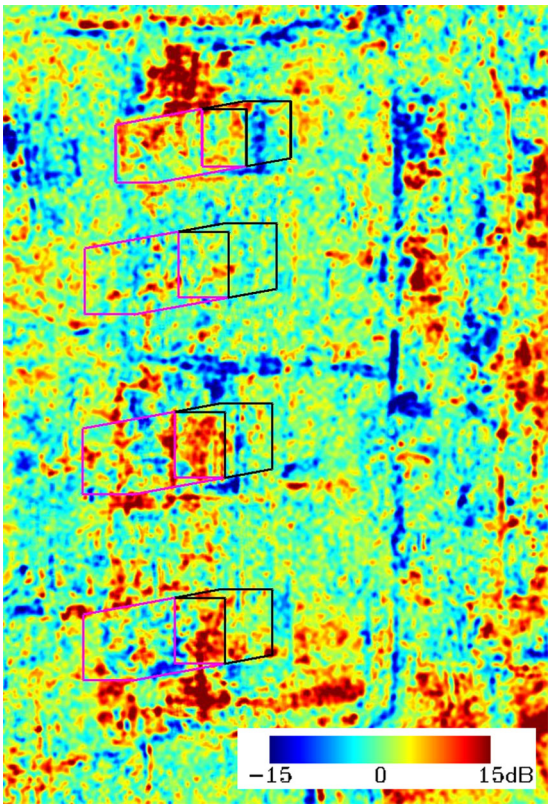

Fig. 8. Difference of the backscatter intensity between the SAR image taken on March 11, 2011 and September 7, 2013 (d =2013-2011).

Table 4. The average values of the difference within layover, footprint and radar shadow areas of the R/Bs for the units 1–4 [dB].

Dimension	Unit 1	Unit 2	Unit 3	Unit 4
Layover	3.15	0.35	2.22	0.45
Footprint	2.59	0.93	5.71	5.10
Radar shadow	-1.60	-0.29	0.01	3.07

7. Conclusions

We used four high-resolution X-band SAR satellite images to detect damage in reactor buildings at the Fukushima Daiichi NPP. No pre-event SAR images existed that were taken under the same acquisition conditions as post-event images, so we built backscattering models and compared them to observed SAR intensity images. Based on comparisons of the damaged unit 1 R/B and the undamaged unit 2 R/B, we summarized criteria for detecting building damage. We used the strongest corner reflection as the first criterion for evaluating the existence of target building outer walls in the sensor direction. Backscattering patterns on two sides of the corner reflection within the layover were useful in detecting the collapse of the upper part and damage to the wall. We also linked backscattering in the radar shadow area to changes in building height.

We discussed the damage situation of units 3 and 4 using these criteria. Using the simulated backscattering model for unit 2, we observed collapse of the tops of unit 3 and the disappearance of the concrete cover on the seaside for both units 3 and 4. Compared to optical satellite images taken by WV-2, we found high-resolution SAR images to be highly capable of detecting damage situations for both roofs and walls. Based on comparisons of the three SAR images taken during the same month under different acquisition conditions, we found that observation from the east side was more suitable for detecting damage to reactor buildings in this case.

Note that this study is a preliminary attempt in damage detection from a single high-resolution SAR intensity image. Backscattering models were built manually based on geometric features without considering material properties, so there are slight differences between our model and actual SAR images, but these models could potentially be used for detailing damage detected in a single building. The model would be improved by introducing SAR simulation algorithms and additional information.

Further comparisons of the backscattering model and actual SAR intensity images are likely to be carried out, so a database of backscattering patterns and different types of building damages will be built to estimate building damage levels automatically.

Acknowledgements

TerraSAR-X/TanDEM-X images used in this study are property of DLR and distributed by Airbus DS/Infoterra GmbH. They were provided for this work through the PASCO Corporation. WorldView-2 images are the property of Digital Globe Inc. This study was supported financially by a grant-in-aid for Scientific Research (project numbers 15K16305 and 24241059), and by a Core Research for Evolutional Science and Technology (CREST) program "Establishing the most advanced disaster reduction management system by fusion of real-time disaster simulation and big data assimilation" sponsored by the Japan Science and Technology Agency (JST) under Research Director Prof. Shunichi Koshimura of Tohoku University.

References:

[1] Prime Minister of Japan and His Cabinet, "Report of Japanese Government to the IAEA Ministerial Conference on Nuclear Safety – The Accidentat TEPCO's Fukushima Nuclear Power Stations –," pp. IX-10, 2011, available at: http://japan.kantei.go.jp/kan/topics /201106 /iaea_houkokusho_e.html [accessed Feb. 15, 2016]

[2] K. Saito, R. J. S. Spence, C. Going, and M. Markus, "Using High-Resolution Satellite Images for Post-Earthquake Building Damage Assessment: A Study Following the 26 January 2001 Gujarat Earthquake," Earthquake Spectra, Vol.20, No.1, pp. 145-169, 2004.

[3] F. Yamazaki, Y. Yano, and M. Matsuoka, "Visual Damage Interpretation of Buildings in Bam City Using QuickBird Images Following the 2003 Bam, Iran, Earthquake," Earthquake Spectra, Vol.21, No.S1, pp. 329-336, 2005.

[4] X. Tong, Z. Hong, S. Liu, X. Zhang, H. Xie, Z. Liu, S. Yang, W. Wange, and F. Bao, "Building-damage detection using pre- and post-seismic high-resolution satellite stereo imagery: A case study of the May 2008 Wenchuan earthquake," ISPRS J. Photogramm. Remote Sens., Vol.68, pp. 13-27, 2012.

[5] G. Taskin, O. K. Ersoy, and M. E.Kamasak, "Earthquake-induced damage classification from postearthquake satellite image using spectral and spatial features with support vector selection and adaptation," J. Appl. Remote Sens., Vol.9, No.1, pp. 096017, 2015.

[6] S. Plank, "Rapid damage assessment by means of multi-temporal SAR – A comprehensive review and outlook to Sentinel-1," Int. J. Remote Sens., Vol.6, pp. 4870-4906, 2014.

[7] M. Matsuoka and M. Estrada, "Development of earthquake-induced building damage estimation model based on ALOS/PALSAR observing the 2007 Peru earthquake," Journal of Disaster Research, Vol.8, No.2, pp. 346-355, 2013.

[8] W. Liu, F. Yamazaki, B. Adriao, E. Mas, and S. Koshimura, "Development of building height data in Peru from high-resolution SAR imagery," Journal of Disaster Research, Vol.9, No.6, pp. 1042-1049, 2014.
[9] W. Liu, F. Yamazaki, H. Gokon, and S. Koshimura, "Extraction of Tsunami Flooded Areas and Damaged Buildings in the 2011 Tohoku-oki, Japan Earthquake from TerraSAR-X Intensity Images," Earthquake Spectra, Vol.29, No.S1, pp. S183-2000, 2013.
[10] D. Brunner, G. Lemoine, and L. Bruzzone, "Earthquake damage assessment of buildings using VHR optical and SAR imagery," IEEE Trans. Geosci. Remote Sens., Vol.48, No.5, pp. 2403-2420, 2010.
[11] T. L. Wang and Y. Q. Jin, "Postearthquake building damage assessment using multi-mutual information from pre-event optical image and postevent SAR image," IEEE Geosci. Remote Sens. Lett., Vol.9, No.3, pp. 452-456, 2012.
[12] Tokyo Electric Power Company (TEPCO), http://www.tepco.co.jp/nu/fukushima-np/f1/genkyo/index-j.html [accessed Feb. 15, 2016]
[13] R. Welch and W. Ehlers, "Merging Multiresolution SPOT HRV and Landsat TM Data," Photogrammetric Engineering & Remote Sensing, Vol.53, No.3, pp. 301-303, 1987.
[14] Deutsches Zentrum für Luft- und Raumfahrt (DLR), http://www.dlr.de/hr/en/desktopdefault.aspx/tabid-2317/3669_read-5488/ [accessed Feb. 15, 2016]
[15] A. Lopes, R. Touzi, and E. Nezry, "Adaptive Speckle Filters and Scene Heterogeneity," IEEE Trans. Geosci. Remote Sens., Vol.28, No.6, pp. 992-1000, 1990.
[16] Y. Fuji-ie, "A Message 15 Days After the 3.11 Earthquake on the Nuclear Accident at Fukushima #1 NPS," Journal of Disaster Research, Vol.7, No.sp, pp. 426-431, 2012.
[17] Geospatial Information Authority of Japan (GSI), http://saigai.gsi.go.jp/h23taiheiyo-hr/index.html [accessed Feb. 15, 2016]
[18] Y. Iwasaki, F. Yamazaki, W. Liu, T. Nonaka, and T. Sasagawa, "Detection of damage to building side-walls using high resoltuion satellite SAR images," Journal of Japan Association for Earthquake Engineering, Vol.13, No.5, pp. 18-32, 2013 (in Japanese).
[19] F. Yamazaki, Y. Iwasaki, W. Liu, T. Nonaka, and T. Sasagawa, "Detection of damage to building side-walls in the 2011 Tohoku, Japan earthquake using high-resolution TerraSAR-X images," Proc. of SPIE, Vol.8892, 889212 1-9, 2013.
[20] F. Yamazaki and W. Liu, "Urban Change Monitoring: Multitemporal SAR Images," Encyclopedia of Earthquake Engineering, Springer, 2014.
[21] B. Adriano, E. Mas, S. Koshimura, H. Gokon, W. Liu, and M. Matsuoka, "Developing a method for urban damage mapping using radar signtures of building footprint in SAR imagery: A case study after the 2013 super typhoon Haiyan," Proc. IEEE IGARSS 2015, pp. 3579-3582, 2015.

Name:
Wen Liu

Affiliation:
Assistant Professor, Graduate School of Engineering, Chiba University

Address:
1-33 Yayoi-cho, Inage-ku, Chiba 263-8522, Japan

Brief Career:
2010-2013 Ph.D. of Engineering, Chiba University
2013-2014 JSPS Postdoctoral Fellowship for Foreign Researchers, Tokyo Institute of Technology
2014 Assistant Professor, Graduate School of Engineering, Chiba University

Selected Publications:
• "Extraction of Tsunami Flooded Areas and Damaged Buildings in the 2011 Tohoku, Japan Earthquake from TerraSAR-X Intensity Images," Earthquake Spectra, ERRI, Vol.29, No.S1, pp. S183-2000, 2013.

Academic Societies & Scientific Organizations:
• Japan Society of Civil Engineers (JSCE)
• Remote Sensing Society of Japan (RSSJ)
• Institute of Electrical and Electronics Engineers (IEEE)

Name:
Fumio Yamazaki

Affiliation:
Professor, Department of Urban Environment Systems, Chiba University

Address:
1-33 Yayoi-cho, Inage-ku, Chiba 263-8522, Japan

Brief Career:
1978 Research Engineer, Shimizu Corporation, Japan
1989 Associate Professor, Institute of Industrial Science, University of Tokyo
2001 Professor, Asian Institute of Technology (AIT), Bangkok, Thailand
2003 Professor, Department of Urban Environment Systems, Chiba University

Selected Publications:
• W. Liu and F. Yamazaki, "Detection of Crustal Movement from TerraSAR-X intensity images for the 2011 Tohoku, Japan Earthquake," Geoscience and Remote Sensing Letters, Vol.10, No.1, pp. 199-203, 2013.
• A. Meslem, F. Yamazaki, and Y. Maruyama, "Accurate evaluation of building damage in the 2003 Boumerdes, Algeria earthquake from QuickBird satellite images," Journal of Earthquake and Tsunami, Vol.5, No.1, pp. 1-18, 2011.

Academic Societies & Scientific Organizations:
• Japan Society of Civil Engineers (JSCE)
• American Society of Civil Engineering (ASCE)
• Seismological Society of America (SSA)
• Earthquake Engineering Research Institute, USA (EERI)

Name:
Tadashi Sasagawa

Affiliation:
Director, PASCO Corporation

Address:
Meguro Bekkan Bldg, 2-8-10 Higashiyama, Meguro-ku, Tokyo 153-0043, Japan

Brief Career:
1982 Master of Engineering, Hokkaido University
1982- PASCO Corporation
2005 Ph.D. of Engineering, Hokkaido University

Selected Publications:
• "Estimation of three-dimensional crustal movements in the 2011 Tohoku-oki, Japan earthquake from TerraSAR-X intensity images," Natural Hazards and Earth System Sciences, Vol.15, pp. 637-645, 2015.

Academic Societies & Scientific Organizations:
• Remote Sensing Society of Japan (RSSJ)
• Japan Society of Photogrammetry and Remote Sensing (JSPRS)
• GIS Association of Japan (GISA)